Publication IV

O. Trushin, J. Jalkanen, E. Granato, S. C. Ying, and T. Ala-Nissila. 2009. Atomistic studies of strain relaxation in heteroepitaxial systems. Journal of Physics: Condensed Matter, volume 21, number 8, 084211, 13 pages. doi:10.1088/0953-8984/21/8/084211.

J. Phys.: Condens. Matter **21** (2009) 084211 (13pp) doi:10.1088/0953-8984/21/8/084211

Atomistic studies of strain relaxation in heteroepitaxial systems

O Trushin[1], J Jalkanen[2], E Granato[3,4], S C Ying[4] and T Ala-Nissila[2,4]

[1] Institute of Physics and Technology, Yaroslavl Branch, Academy of Sciences of Russia, Yaroslavl 150007, Russia
[2] Department of Engineering Physics, Helsinki University of Technology, FIN-02015 TKK, Espoo, Finland
[3] Laboratório Associado de Sensores e Materiais, Instituto National de Pesquisas Espaciais, 12227-010 São José dos Campos, SP, Brazil
[4] Department of Physics, Brown University, Providence, RI 02912, USA

Received 18 July 2008
Published 30 January 2009
Online at stacks.iop.org/JPhysCM/21/084211

Abstract
We present a review of recent theoretical studies of different atomistic mechanisms of strain relaxation in heteroepitaxial systems. We explore these systems in two and three dimensions using different semi-empirical interatomic potentials of Lennard-Jones and many-body embedded atom model type. In all cases we use a universal molecular static method for generating minimum energy paths for transitions from the coherent epitaxial (defect free) state to the state containing an isolated defect (localized or extended). This is followed by a systematic search for the minimum energy configuration as well as self-organization in the case of a periodic array of islands. In this way we are able to understand many general features of the atomic mechanisms and energetics of strain relaxation in these systems. Finally, for the special case of Pd/Cu(100) and Cu/Pd(100) heteroepitaxy we also use conventional molecular dynamics simulation techniques to compare the compressively and tensilely strained cases. The results for this case are in good agreement with the existing experimental data.

(Some figures in this article are in colour only in the electronic version)

1. Introduction

Heteroepitaxial systems play an important role in modern microelectronics technology [1]. Due to the lattice mismatch between the film and the substrate, considerable elastic strain energy is accumulated in epitaxy. For sufficiently thick films, defects will form leading to the relaxation of strain energy and to the loss of coherent epitaxy [2]. Controlling the film–substrate interface quality and preventing defect formation is an important problem of modern technology. Experimental methods at present do not allow either a detailed study of the defect core at the atomic level or the time evolution of the system during defect nucleation process. Therefore, theoretical modeling plays an important role in the studies of defect core structures and the mechanisms of their formation.

Misfit dislocations are the most important type of defects in heteroepitaxial systems [3]. Early theoretical studies of misfit dislocations were based on the comparison of equilibrium energies for configurations with and without dislocations [4, 5]. Recently it has been recognized that the formation of defects leading to the loss of coherent epitaxy is a thermally activated process, which is supported by the experimentally observed temperature dependence of the critical thickness of the film. It follows then that the state of the epitaxial system that is seen in the experiments is determined not just by the nature and energy of the final state but also by the kinetic factors dependent on the nature of the entire transition path, and in particular by the energy barrier required to cross the relevant saddle point controlling strain relaxation.

We have recently explored the detailed relaxation mechanisms at the microscopic scale for generic two-dimensional (2D) and three-dimensional (3D) heteroepitaxial systems [6–9]. Starting from the initial epitaxial state, we generate the final configuration containing different kinds of defects with the repulsive bias potential method (RBP) [10]. Then the nudged elastic band method [11] is employed to determine the minimum energy transition path. This approach allows us to systematically classify the atomic

mechanisms leading to strain relaxation in 2D and 3D systems. Among the central findings is a strong asymmetry between compressive and tensile overlayers, highlighting the importance of anharmonic effects. In addition to studying the general features of heteroepitaxial systems, this approach in conjunction with traditional molecular dynamics simulation techniques has been applied to the specific system of Cu–Pd heteroepitaxy on a fcc(100) geometry [12]. There, the theoretical results are in excellent quantitative agreement with experimental observations for both the compressively strained Pd on Cu and the tensilely strained Cu on Pd systems. In this work we present a brief review of these studies together with some recent new results for 3D systems.

Another possible path to strain relaxation for heteroepitaxial system is through the spontaneous formation of a periodic array of isolated islands in the so-called 'Stranski–Krastanov' or 'Volmer–Weber' growth regimes. This channel of strain relaxation competes with the dislocation mechanisms and the easiest path for a given system depends on the details of the system parameters. In this review we will discuss these two mechanisms separately.

2. Interatomic potentials

Our first goal is to understand the qualitative features of strain relaxation mechanisms that are not dependent on the details of the interatomic potentials. For this purpose, we study generic systems for which the interactions between atoms are modeled by a generalized Lennard-Jones (LJ) pair potential [22] of the form:

$$V(r) = \varepsilon \left[\frac{m}{n-m} \left(\frac{r_0}{r}\right)^n - \frac{n}{n-m} \left(\frac{r_0}{r}\right)^m \right] \Theta(r), \qquad (1)$$

where

$$\Theta(r) = \begin{cases} 1, & r \leqslant r_0; \\ 3\left(\dfrac{r_c - r}{r_c - r_0}\right)^2 - 2\left(\dfrac{r_c - r}{r_c - r_0}\right)^3, & r_0 \leqslant r \leqslant r_c; \\ 0, & r_c \leqslant r. \end{cases} \qquad (2)$$

and r is the interatomic distance, ε the dissociation energy, r_c the potential cut-off radius and r_0 the equilibrium distance between the atoms. The same kind of potential with $m = 12$ and $n = 6$, has been used previously in a similar context by Dong *et al* [23] in a molecular dynamics simulation study of a 2D model for the growth of strained epitaxial films. In most of our calculations we use the values $n = 5$ and $m = 8$. In contrast to the usual 6–12 potential, this has a slower fall-off. By varying the cut-off radius r_c, we can explore how the results depend on the range of the potential. The cut-off function Θ ensures that the potential and its first derivative vanish beyond the cut-off r_c. The equilibrium interatomic distance r_0 was set to a different value r_{ss}, r_{ff} and r_{fs} for the substrate, film and film–substrate interactions, respectively. The parameter r_{ff} was determined by the misfit between lattice parameters as

$$f = (r_{ff} - r_{ss})/r_{ss}. \qquad (3)$$

For the film–substrate interaction, we set the equilibrium distance r_{fs} to the average of the film and substrate lattice constants, i.e. $r_{fs} = (r_{ff} + r_{ss})/2$. A positive mismatch $f > 0$ corresponds to compressive strain and negative to tensile strain when the film is coherent with the substrate.

Using the generalized LJ model allows us to decouple parameters such as misfit value and bond energy, which considerably simplifies the analysis. For more accurate description of bimetallic systems, we have also done studies for specific heteroepitaxial systems where the interatomic forces between particles are modeled by many-body embedded atom model (EAM) potentials [24]. Within EAM the total energy of a many-atom system is written as a sum of two terms: a repulsive part and an attractive part, which are given by

$$U = \sum_{i<j} \varphi_{ij}(r_{ij}) + \sum_i F_i[\rho(\vec{r}_i)]. \qquad (4)$$

The repulsive part represents the sum of screened Coulomb interactions between all atomic pairs

$$\varphi_{ij}(r) = \frac{Z_i(r) Z_j(r)}{r}, \qquad (5)$$

where the effective charge is written as follows:

$$Z_i(r) = Z_0^i (1 + \beta r^\nu) \exp(-\alpha r). \qquad (6)$$

The attractive energy is calculated as a sum over embedding functions centered at the atomic positions. It depends on total electronic density at the position of given atom as

$$\rho(\vec{r}_i) = \sum_{j \neq i} \rho_{at}\left(\left|\vec{r}_i - \vec{r}_j\right|\right). \qquad (7)$$

This term implicitly contains many-body interactions through the total electronic density $\vec{r}_i$.

We have applied the EAM potential to bimetallic systems for a combination of elements such as Ni, Pd, Cu, and Ag. In addition to providing a realistic picture of these systems, comparison of models with EAM and LJ potentials allows us to separate the general features that are not sensitive to the details of the potential from those that can change even qualitatively depending on the interatomic potentials.

3. Strain relaxation through isolated dislocations

3.1. Method for generating transition paths to isolated dislocations

To study the transition path of a strained system from an initial epitaxial state to a final state which contains an isolated defect, we need to employ some kind of an activation procedure. The simplest way is through heating and thermalization at a given temperature. The standard way of thermally generating transition paths through molecular dynamics (MD) simulations [13] does not work well in cases where the probability for rare activated events is small. Additionally, at high temperatures many different defects typically appear at the same time, which makes it complicated to understand the formation energetics of each specific defect in detail.

To clarify the picture of defect generation we need to use a more controlled way to activate the relaxation to avoid the creation of mixtures of different defects. There are now numerous methods which have been constructed to solve this fundamental problem. The MD technique itself has been augmented by various acceleration [14], sampling [15, 17] and coarse graining schemes [16]. In addition, there is a class of methods that does not evaluate the dynamics directly but instead focuses on a systematic search of transition paths and related saddle points for many-particle systems [18–21].

We have recently introduced [10] a particularly simple but efficient method called the repulsive bias potential (RBP) method for transition path searching. In the RBP method, the system is placed in a fixed external repulsive bias potential which makes the initial state unstable but keeps the other nearby minima unaffected:

$$U_{\mathrm{tot}}(\vec{r}, \vec{r}_0) = U(\vec{r}) + A \exp\{-[(\vec{r} - \vec{r}_0)/\alpha]^2\}. \qquad (8)$$

Here the components of $\vec{r}_0$ and $\vec{r}$ contain all the coordinates of the initial and current configurations, respectively. The term $U(\vec{r})$ contains the mutual interactions of the particles and the additional term is an exponentially decaying, spherically symmetric potential of strength A, range α and a maximum at $\vec{r}_0$. When A and α have been chosen appropriately, forces computed from equation (8) can displace the system from its initial state sufficiently to make an escape to a nearby minimum to take place. In practice this is done by applying total energy minimization with U_{tot}.

With the RBP method implemented, the procedure of determining the transition path comprises several stages. First, the initial epitaxial state is prepared by minimizing the total energy of the system using MD cooling. In the MD cooling method, the energy is gradually minimized by setting each particle velocity to zero whenever it has a component opposite to the direction of the acceleration. The standard leap-frog algorithm is used to numerically integrate the equations of motion. Following this, we use this initial state to write down a RBP bias. In addition, a small group of particles is slightly displaced from the initial position to bring the system closer to the saddle point of the particular relaxation process that we want to study. After these preparations, the total energy minimization is reapplied.

It is important to note that the RBP method can generate many different final states depending on both the initial displacements and the exact form of the repulsive bias introduced. By making the repulsive bias sufficiently localized around the initial potential minimum, the final state energy depends only on the true potential of the system and not on the fictitious repulsive bias. In our studies, we consider only the final configurations with precisely one isolated dislocation to understand the details of the generation mechanism and the energetics. Rather than trying random initial displacements, some knowledge of the dislocation generation mechanism is useful for expediting the process. For example, in the case of misfit dislocations, we find that the proper choice of initial displacements depends on the sign of the misfit. For compressive strain, to generate an ideal single misfit dislocation *in* the center of our sample, the optimal initial displacement corresponds to moving one atom in the middle of the first layer of the film upwards from the film–substrate interface by a small distance ($0.04r_{\mathrm{ss}}$). For tensile strain, the optimal initial displacement corresponds to moving an atom in the second layer of the film downwards from the film–substrate interface by a similar distance.

While the RBP minimization can be used to generate a configuration containing an isolated dislocation, it does not yield the precise minimum energy path or the lowest activation barrier value for the process connecting the initial and final states. For this purpose, we use the nudged elastic band (NEB) method [11], which is an efficient method for finding the minimum energy path (MEP). The starting point for NEB algorithm is a set of transitional configurations (images) between the known initial and final states. The algorithm then gradually relaxes this path so that in the end all images are samples from the true MEP. An initial guess for the images is usually obtained by interpolating the particle configurations between the final and initial states. For our studies however, we find that this often leads to numerical instabilities due to the strong hard core repulsion of the interatomic potentials. To circumvent this problem, we use the intermediate configurations that we store during the final state search with the repulsive bias as the initial input for NEB. This leads to fast convergence without the instabilities encountered with the linear interpolation scheme.

For epitaxial films above the equilibrium critical thickness, the relaxed state with a nonzero density of dislocations which partially relieves the strain energy in the film is expected to have a lower energy. However, if this configuration is separated from the coherent state by a finite energy barrier ΔE, the film will remain coherent until a sufficiently large energy fluctuation allows a defect to be nucleated. This barrier could be finite even when the relaxed state has already a lower energy than the epitaxial state. Thus the experimentally observed critical thickness can be much larger than the equilibrium value depending on the kinetics of defect nucleation. Our results [6–8] showed a large variety of relaxation processes, including single dislocation nucleation, multiple dislocations, dislocations with different core structures, and dislocations nucleating at different depths in the film, which can be characterized by their different activation energies and energies of the final incoherent states.

3.2. Results for 2D models

In this section, we review the results for generic 2D models where the interatomic potentials are modeled by the generalized LJ potentials as described in the earlier section. We focus here on the nucleation and MEP leading to a final state containing only a single misfit dislocation with core located near the film–substrate interface. To simplify the discussion, we will present here only the results for the 5–8 potential with a cut-off radius of $r_{\mathrm{c}} = 1.5r_{\mathrm{ss}}$, and lateral size $L = 50r_{\mathrm{ss}}$ corresponding to 50 atoms per layer. Calculations were performed with periodic boundary conditions in the direction parallel to the film–substrate interface. For large systems ($L >$ 200), free boundary conditions gave qualitative similar results.

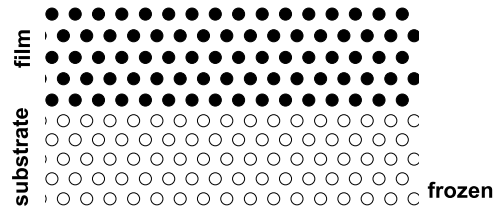

Figure 1. A schematic figure of the 2D model of the epitaxial film and substrate showing the particle configurations in the coherent state. The two layers at the bottom are held fixed while all others are free to move. Filled circles represent the epitaxial film and open circles the substrate. Reproduced from [8]. Copyright 2003 by the American Physical Society.

In the calculations, the two bottom layers of the five-layer substrate were held fixed to simulate a semi-infinite substrate while all other layers were free to move. The central portion of the initial epitaxial film and substrate are shown in figure 1. These choices of the system size and parameters allow us to arrive at a simple physical picture for the nucleation process of the misfit dislocation in the generic 2D model. The results with different parameters for the intermolecular potential and different size of the system are qualitatively similar. For both the compressive and tensile strain cases, we find a finite activation barrier ΔE on the MEP leading from the initial epitaxial state to the final state with a single misfit dislocation in the film–substrate interface.

To visualize the energy profile along a MEP, we introduce a reaction coordinate S_M. We take it to be the accumulated displacement of the system along the transition path,

$$S_M = \sum_{m=1}^{M} \sqrt{\sum_{i=1}^{N} (r_i^m - r_i^{m-1})^2 / N}. \qquad (9)$$

Here m is the label for the configuration (image) under consideration, and i is the index for the different particles in the system ($i = 1$–N). In figures 2 and 3, we show typical snapshots of configurations along the corresponding MEP for compressive and tensile films, respectively. In all cases the initial state was an epitaxial film with a coherent interface and the final state contained a single dislocation with its core located in the interface layer. The final state is characterized by the presence of an adatom island on the surface of the film in the case of compressive strain and a vacancy island in the tensile case. The number of adatoms (or vacancies) in the single layer thick island is exactly the number of layers in the film. Such form of the final state is determined by the geometry of the lattice, as the one extra atom needs to be added to or removed from each layer to relax the strain.

The NEB method usually converges to the MEP nearest to the initial trial trajectory. Thus by changing the initial input path, we were able to investigate several different mechanisms of relaxation [6–8]. These mechanisms differ from each other mainly by the level of collectiveness in the displacement of the particles from the coherent state position. For each given set of parameters, we identify the lowest activation barrier. The particular kind of mechanism leading to the lowest barrier

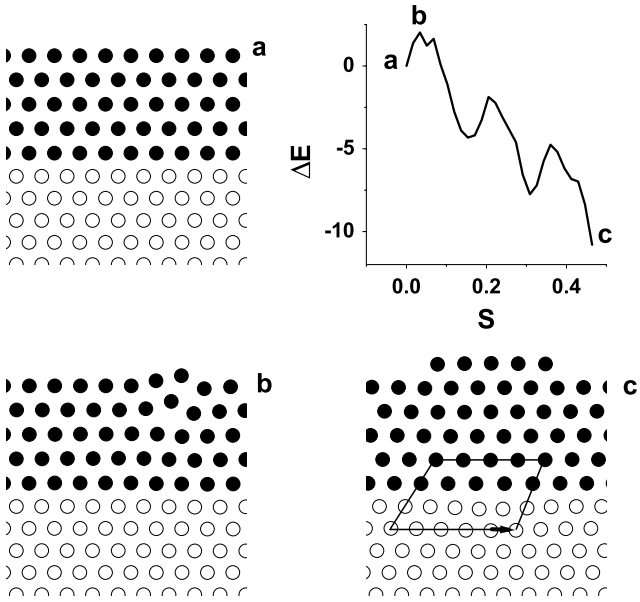

Figure 2. Minimum energy path [8] for compressive strain $f = +8\%$ as a plot of the energy barrier ΔE versus the reaction coordinate. Snapshot configurations (a), (b) and (c) correspond to the labels in the energy profile (top right). The closed line in (c) is the Burgers circuit around the dislocation core. The energy barrier is in units of interatomic potential strength ε and the reaction coordinate S is in units of equilibrium distance r_{ss}. Reproduced from [8]. Copyright 2003 by the American Physical Society.

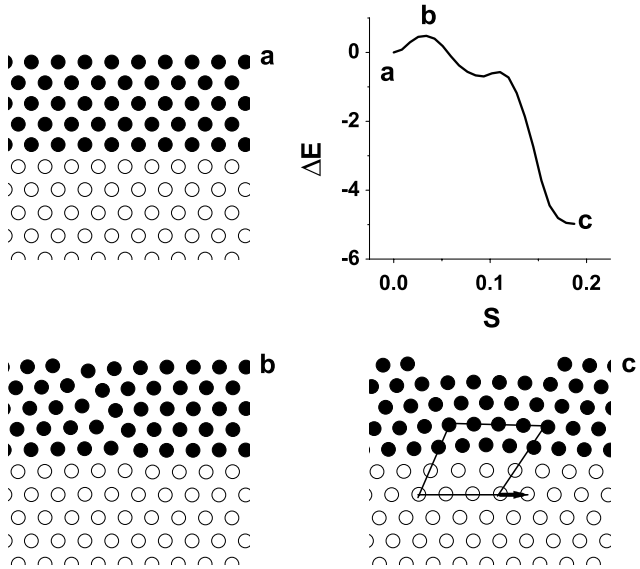

Figure 3. Minimum energy path [8] for tensile strain $f = -8\%$ as a plot of the energy barrier ΔE versus the reaction coordinate S. Snapshot configurations (a), (b) and (c) correspond to the labels in the energy profile (top right). The closed line in (c) is the Burgers circuit around the dislocation core. The energy barrier is in units of interatomic strength ε and the reaction coordinate S in units of equilibrium distance r_{ss}. Reproduced from [8]. Copyright 2003 by the American Physical Society.

depends on the parameters of the model (misfit, cut-off radius of potential etc). We found that for all the 2D systems that we studied, the mechanisms leading to the lowest activation barrier belong to one of the two categories described below.

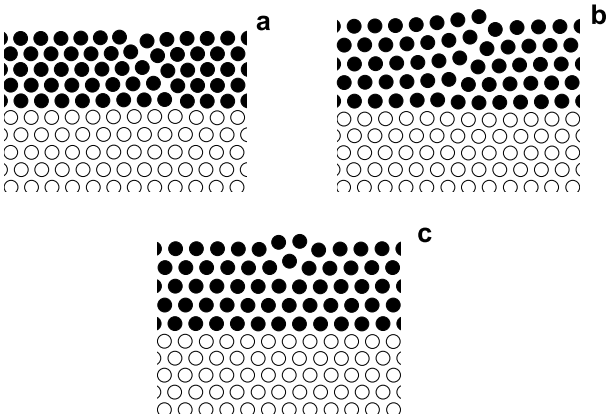

Figure 4. Saddle point configurations for different mechanisms [8] of stress relaxation in 2D: (a) glide mechanism for tensile strain; (b) glide mechanism for compressive strain, and (c) climb mechanism for compressive strain. Filled circles represent the epitaxial film and open circles the substrate. Reproduced from [8]. Copyright 2003 by the American Physical Society.

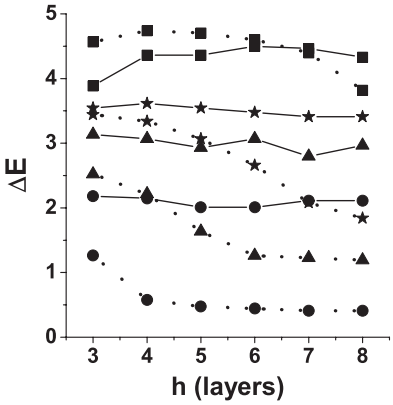

Figure 5. The energy barrier ΔE (in units of ε) as a function of the film thickness (number of layers) for different misfit values [8]. Squares correspond to $f = \pm 4\%$, stars to $f = \pm 5\%$, triangles to $f = \pm 6\%$, and circles to $f = \pm 8\%$. Solid and dotted lines correspond to compressively $f > 0$ and tensilely $f < 0$ strained overlayers, respectively. Reproduced from [8]. Copyright 2003 by the American Physical Society.

The first mechanism describing the transition from the initial coherent state to the final state with a misfit dislocation at the film–substrate interface corresponds to a successive sliding along the edges of a triangle. The saddle point configurations corresponding to this mechanism for the tensile and compressive strain cases are shown in figures 4(a) and (b), respectively. We see that in this case the displacements of the atoms have collective behavior, with two edges of a triangle successively sliding up or down (one by one). Eventually, an adatom island or a vacancy island is created on the surface of the film. The lowest saddle point can correspond either to the sliding of the first or the second edge. We refer to this as the glide mechanism since the motion of the dislocation after it is nucleated follows the path referred in the literature as dislocation glide [25]. For the tensile strain case, the glide mechanism always yields the lowest activation barrier. For the compressively strained film, the mechanism leading to the lowest activation barrier depends on the magnitude of the misfit. For small misfits ($f \leqslant 8\%$), the glide mechanism is again the one leading to the lowest activation barrier. This is drastically different from the climb mechanism reported earlier [6] for a misfit of 8% in a compressively strained film.

The second mechanism corresponds to a successive descending of a misfit dislocation from layer to layer. This is the preferred mechanism for a compressively strained film with large misfits ($f \geqslant 8\%$). The saddle point configuration corresponding to this mechanism for the compressive strain of 8% misfit is shown in figure 4(c). In this case, the core of the dislocation first appears at either the second or the third layer of the film and then successively moves down from layer to layer to the film–substrate interface. The displacement of the particles have a very localized character in this kind of mechanism. We refer to this as the climb mechanism since the motion of the dislocation after it is first nucleated in this case corresponds to what is known in the literature as dislocation climb [25]. For intermediate values of compressive strain, the situation is more complicated, as the two mechanisms are competitive in energy cost. The actual MEP in this case is better described by a mixture of the climb and glide mechanisms.

The most important characteristic of a particular relaxation process through nucleation of a misfit dislocation is its activation energy ΔE. The activation barrier is calculated as the difference between the total energy of the initial state and that of the saddle point configuration. As can be seen in figure 2, corresponding to the compressively strained case, there may exist many saddle points along a given MEP. The activation barrier is determined by the lowest energy saddle point. The results for ΔE versus the number of layers in the film are presented in figure 5.

For the tensile strain case, we find that the process leading to the nucleation of misfit dislocation and subsequent motion along the MEP is always through the glide mechanism. The activation barrier decreases with increasing magnitude of misfit. Also, at large misfits, the activation barrier decreases significantly as the film thickness increases, leading to an essentially negligible activation barrier. This was verified directly through independent MD simulations at finite temperatures where the misfit dislocation is easily generated spontaneously.

For the compressive strain case, except at 4% misfit and small thickness (less than six layers), the barriers are higher than in the corresponding tensile strain case with the same magnitude of misfit. Again, there is a strong decrease in ΔE with increasing magnitude of misfit. In contrast to the tensile strain case, the activation barrier tends to level off with increasing film thickness. The other striking difference from the tensile strain case is that the mechanism corresponding to the movement along the MEP in this case can either be the glide mechanism as in the tensile strain case, or the qualitatively totally different climb mechanism involving layer by layer distortion as discussed in the last section. This new climb mechanism occurs for large misfits ($f \geqslant 8\%$).

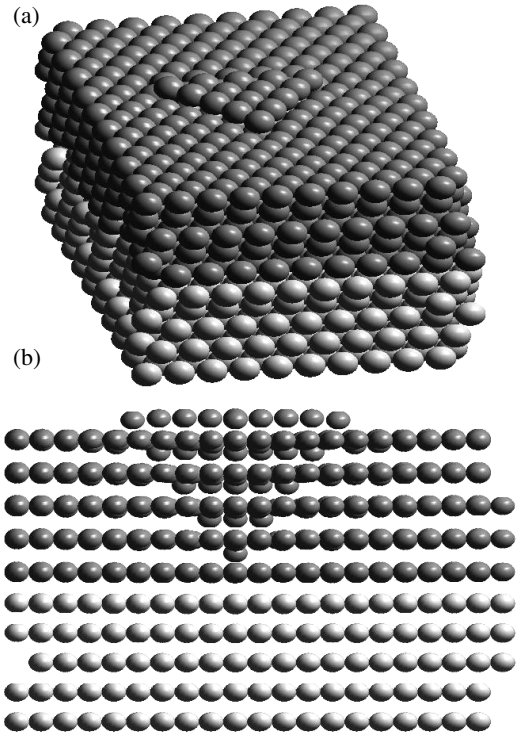

Figure 6. Final relaxed state in the case of a localized stacking fault tetrahedron for the compressively strained 3D LJ system with $f = 8\%$. (a) Top view of the final state with a 2D triangular island. (b) Side view of the structure of the tetrahedron.

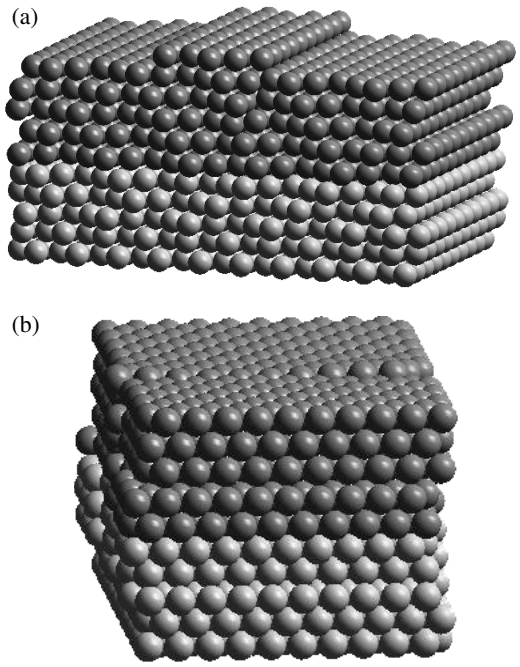

Figure 7. Final relaxed state in the case of an ideal misfit dislocation for the compressively strained 3D LJ system with $f = 8\%$. (a) Final state with a 2D extended island—signature of a misfit dislocation. (b) Saddle point configuration for dislocation nucleation.

3.3. Results for 3D models

3.3.1. Generic LJ models for fcc(111) interface. In this section we present new, unpublished results for generic 3D systems. To this end, we follow our previous work in 2D [6–8], in choosing the same generalized LJ pair potential [22] for the interatomic potential. In this case we use two different cut-offs: in the so-called short-range (SR) case $r_c = 4$ Å, and in the long-range (LR) case $r_c = 5$ Å. Our 3D model system has the fcc(111) geometry consisting of five atomic layers of substrate and a variable number of film layers (1–10) with lateral sizes of 20×20 atomic rows. Periodic boundary conditions are applied in the plane parallel to the substrate surface. Two bottom layers of the substrate are fixed to simulate a semi-infinite substrate and to prevent the system from moving as a whole.

As our first major result, we find that using the combined RBP activation and minimization procedure we are able to generate *both* localized *and* extended defects in 3D. First, in order to activate a localized defect in a compressively strained system we moved a single atom at the interface slightly upwards (0.1–1.0 Å) and then turned on the RBP. In figures 6(a) and (b) we show a typical example of a localized defect obtained in a compressively strained system with $f = 8\%$. This type of defect is known as the stacking fault tetrahedron [26], and in this case the relaxation process occurs by the upward motion of a tetrahedron, until there is a 2D triangular island on the surface. The number of atoms on each side of the island exactly corresponds to the number of strained overlayers here. This is analogous to the compressively strained 2D case, where a 1D adatom island forms the final relaxed state with the number of adatoms equal to the layer thickness due to geometric reasons [6, 7], as discussed in the previous section.

Existence of these type of localized defects in heteroepitaxial systems has been experimentally confirmed [27]. Although such local defects are in general less effective in releasing strain and usually have a high activation energy barrier, this type of relaxation can compete with extended defect formation in cases where the dislocation formation is suppressed through, e.g., surface patterning [27][5].

To activate extended defects (such as an edge dislocation), we move the whole row of atoms in the interface layer either upwards or downwards depending on sign of the misfit and then turn on the RBP procedure. In figure 7(a) we show a typical example of an edge dislocation obtained in a compressively strained system, again with $f = 8\%$. In this case, the final state configuration is characterized by the appearance of an extended mono-atomic island on the surface. Again, the width of the island exactly corresponds to the thickness of the film, in analogy to the single row of atoms observed in the 2D case [6, 7]. Our calculations show that such an extended defect releases much more strain energy than a local defect discussed above, and has a lower activation barrier for the same system size. The dislocation nucleation process here begins from the creation of a localized defect, which means that the energy barrier does not depend on the

[5] For $f = 8\%$ we found that for the SR potential the energy barrier for localized defect formation is 0.63 r.u., and zero for misfit dislocation formation. However, for the LR case the situation is opposite 2.23 r.u. versus 2.66 r.u.

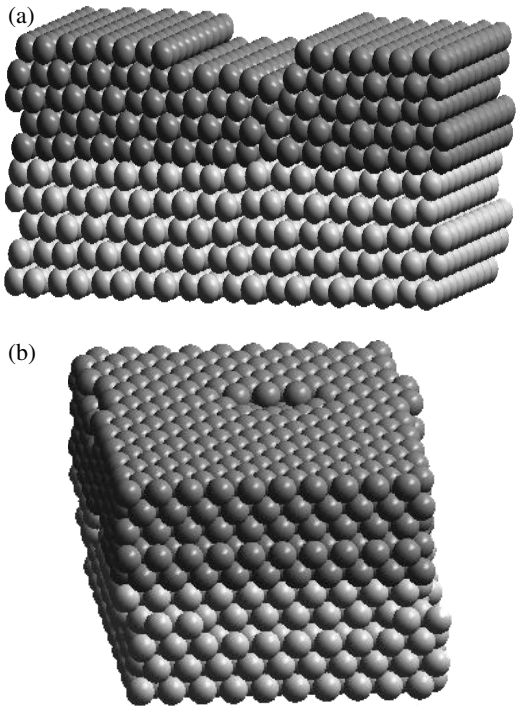

Figure 8. Final relaxed state in the case of an ideal misfit dislocation for the 3D tensile case with $f = -8\%$. (a) Final state with a 2D extended vacancy island—signature of a misfit dislocation. (b) Saddle point configuration for dislocation nucleation.

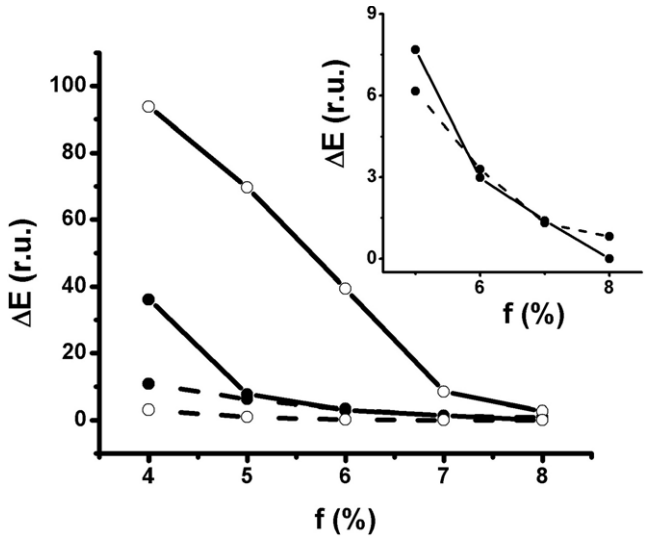

Figure 9. The energy barrier as a function of the misfit for compressively (solid line) and tensilely strained overlayers (dashed line). The data for short cut-off ($r_c = 4$ Å) potential are marked with black circles and for long cut-off ($r_c = 5$ Å) with open circles. The inset shows the nontrivial behavior of the SR case for large misfits. See the text for details.

lateral system size. In figure 7(b) we show the saddle point configuration controlling the dislocation formation. At the first stage a small bump appears on the surface, which then extends and forms a partial dislocation. This is followed by upward motion of the next rows of atoms, until finally the complete island is formed.

It is interesting to compare the above scenario to the tensile case. We find that in analogy to the 2D case, there is a vacancy island (depression) that forms on the surface, as can be seen in figure 8(a), with the step width corresponding to the layer thickness. At the beginning of the dislocation nucleation process a small localized depression appears on the surface. This initial perturbation runs across the sample along the dislocation line forming a mono-atomic vacancy island which corresponds to a partial edge dislocation. At the next stages, the consequent vacancy rows are formed. In figure 8(b) we show the saddle point configuration, which again indicates the local nature of the transition state.

Finally, in figure 9 we present a summary of our quantitative results for the activation barriers ΔE for the SR and LR potentials as a function of the misfit parameter f. The first observation is that the energy barrier decreases and the corresponding gain in energy (difference between the final and initial state energy) increases with increasing f. This observation agrees well with our earlier results for 2D systems [6–8]. There is also a strong asymmetry between the compressive and tensile cases, reflecting the strongly anharmonic nature of the atomistic potentials. This is most clearly seen in the fact that for the largest misfit ($f = 8\%$) studied here, the barrier remains finite for the tensile case while it becomes zero for the compressive case. It is interesting to note that this is *opposite* to what happens in the 2D case.

However, perhaps the most interesting result is the nontrivial dependence of the barrier on the cut-off of the potential. For the LR potential, the barrier for the compressive case remains larger than for the tensile case for all values of f here. In contrast, for the SR case there is nontrivial behavior. For all values of misfit less than about 6%, the compressive case has a larger barrier, but for $f \geqslant 7\%$, the barriers are reversed and the tensile case barrier remains finite while the compressive case barrier goes to zero.

3.3.2. EAM models for fcc(111) interface. To check the influence of the form of the interatomic potential on the results for the 3D model as well as providing a more realistic study of bimetallic systems, we have performed studies of dislocation nucleation in various heteroepitaxial bimetallic systems using the EAM potential. In this section, we will discuss some aspects of the results for the Cu–Pd fcc(111) epitaxial systems. We have chosen Pd/Cu(111) as a representative of a compressively strained system with misfit value of $f = 7.6\%$, while the Cu/Pd(111) system represents a tensilely strained film with $f = -7.2\%$. Applying the general activation procedure described above, we were able to activate both types of isolated defects: localized (stacking fault tetrahedron) and extended (ideal misfit dislocation). The qualitative nature of the saddle point configuration, final state configuration and the transition paths are the same as that shown in figures 7 and 8 for the LJ pair potentials. This is why these configurations are not shown here. The decrease of activation barriers with increasing misfit also follows the same trends. These are the universal features that we consider insensitive to the details of the interatomic potentials. However, certain quantitative details of

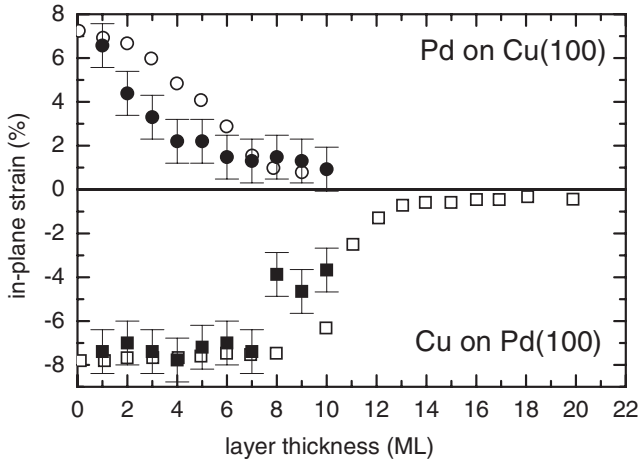

Figure 10. In-plane lattice strain derived from the separation of the first order rods in the RHEED pattern as a function of Pd or Cu coverages. Results from experimental and theoretical work at 300 K are indicated by open and solid symbols, respectively. See the text for details. Reproduced from [12]. Copyright 2005 by the American Physical Society.

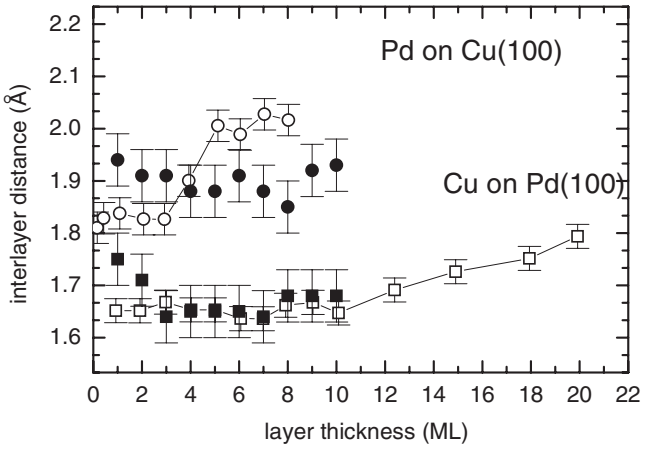

Figure 11. Perpendicular interlayer distance calculated based on a kinetic model from LEED intensity of the (00) diffraction beam versus energy curves. The change of the interlayer distance occurs at about 3–4 ML for Pd/Cu(100) films and at about 10 ML for Cu/Pd(100) films. Assuming a pseudomorphic growth up to 3 ML for Pd on Cu(100) and 10 ML for Cu on Pd(100), PLD films can be identified as fcc Pd and fct Cu structures. The results from experimental and theoretical work at 300 K are indicated by open and solid symbols, respectively. The lines are guides to eye. Reproduced from [12]. Copyright 2005 by the American Physical Society.

the transitions differ considerably between the different types of interatomic potentials. In particular, the actual value of the energy barrier for the transition is very different for different models. In figure 13 we present comparison of energy profiles obtained with various LJ models and the EAM model for the same misfit value $f = 7.6\%$. For each potential, the parameters are adjusted to fit the bulk Pd and Cu, respectively. From this figure we see that the energy profile obtained with the LJ potential systematically approaches that of the EAM potential when the cut-off value for the range of the LJ potential gets smaller, demonstrating that the EAM potential is

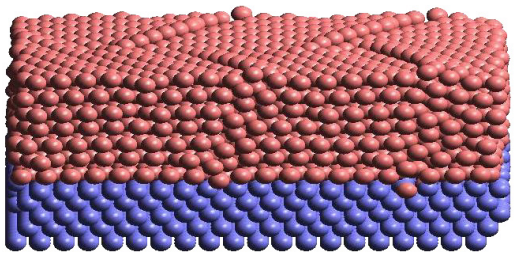

Figure 12. Typical configuration of stacking faults for 7 ML Pd on Cu(100) based on MD annealing. The lateral size is 20×20 atom^2. The misfit dislocations orientate along the ⟨100⟩ direction of the substrate. Reproduced from [12]. Copyright 2005 by the American Physical Society.

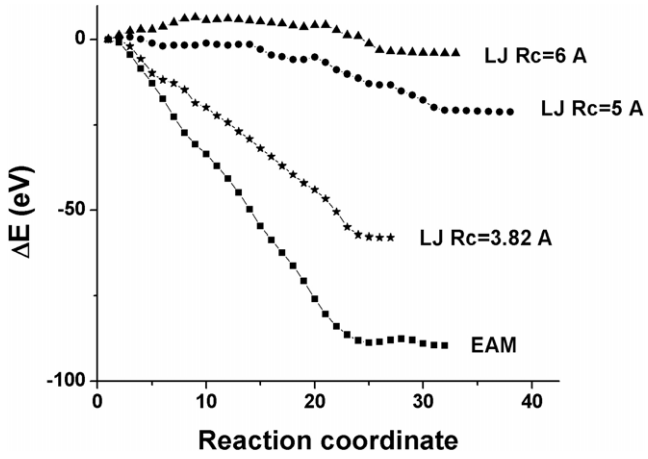

Figure 13. Energy profiles along MEP for different interatomic potentials used for the 3D heteroepitaxial models (r_c is the LJ cut-off parameter). In all cases lateral size of the system was 10×10 atomic rows, substrate thickness 5 ML, and film thickness 5 ML.

effectively a very short ranged interaction in addition to having many-body character.

3.3.3. Results for Pd/Cu(100) and Cu/Pd(100). In this section, we present results from a combined experimental and theoretical study on a model system of Cu–Pd heteroepitaxy [12]. The bulk lattice parameters of Cu and Pd are $a_{Cu} = 3.61$ Å and $a_{Pd} = 3.89$ Å, respectively. The lattice misfit induces a large compressive ($f = 7.8\%$) strain in the Pd overlayer on Cu(100) and a tensile ($f = -7.2\%$) strain for the Cu overlayer on Pd(100). The Pd films on Cu(100) and the Cu films on Pd(100) were grown by pulsed laser deposition (PLD). During deposition the growth process was monitored by reflection high energy electron diffraction (RHEED). The RHEED data analysis for the in-plane strain are shown in figure 10. For Pd/Cu(100), the in-plane stress is relaxed almost immediately above one monolayer (ML), while it persists up to at least 5–6 monolayers in Cu–Pd heteroepitaxy. The most striking discovery in the data is the strong asymmetry in the strain relaxation behavior between the tensilely and compressively strained films. This result is in direct disagreement with the continuum elasticity theory, which predicts symmetrical behavior for tensile and

compressive systems. However, it agrees with the general trends we have found in our study for the generic 2D and 3D systems, as discussed in the previous sections. In addition to the in-plane lattice strain, the perpendicular interlayer distance has also been obtained based on a kinetic model from observed LEED intensity. The data are shown in figure 11.

In any growth mode, there is always the question whether the final configuration is dictated by kinetic considerations or it corresponds to a true thermodynamic equilibrium state. Given the lack of precise characterization of the PLD growth conditions, a full theoretical modeling of the kinetic growth process under the experimental conditions is unfeasible. Instead, we have chosen to perform equilibrium MD simulations of the epitaxial layer after deposition. The object here is to study the thermal excitations and nature of dislocations in the epitaxial film and to see whether they can account for the observed stress relaxation and tensile-compressive asymmetry in the Cu–Pd system. Fortunately, the activation barrier involved for this system is relatively small, so no special schemes such as RBP method described in the earlier section is required to generate the MEP for the dislocations.

Our atomistic model contains five layers of substrate and varying number of film layers. Two bottom layers of the substrate were fixed. Periodic boundary conditions were applied in the plane parallel to the surface. The lateral size of the systems studied varied between 20×20 and 40×40. Interatomic forces between particles in the system were computed using full EAM potentials for Cu and Pd [24]. The initial configuration of the film has adatoms occupying fcc positions in registry with substrate.

For Pd/Cu(100), after thermal equilibrium is reached at 300 K, the system relaxes and gains partial strain relief through generation of misfit dislocations starting at 2 ML and above. To facilitate a direct comparison with the experimental data in figures 10 and 11, we computed from our simulations the average interlayer distance for the top layers of the film (up to three to take into account the surface sensitivity of LEED). We also computed the average in-plane lattice constant for the top three surface layers, and then evaluated the in-plane strain using the bulk value of the adsorbate as a reference. The dependence of these values on the film thickness is shown in figures 10 and 11. There is a good qualitative agreement between the theoretical results with the experimental observation showing continuous relief of in-plane strain through the misfit dislocations. The exact nature of the misfit dislocations is rather complicated, varying both as a function of film thickness and lateral size. In figure 12, we show a typical configuration for a film of 7 ML thickness and lateral size 20×20 obtained by molecular dynamics annealing through heating to 500 K, followed by cooling to 0 K. This shows a Pd film with misfit dislocations visibly aligned along the $\langle 100 \rangle$ direction of the substrate, in agreement with the experimental observations.

Simulation studies were also performed for Cu/Pd(100). Here, in agreement with the experimental observations, the theory shows a striking difference from the Pd/Cu(100) system. The pseudomorphic strained fct structure for the Cu film remains stable up to about 9 ML. Then strain is gradually released through localized surface defects such as vacancies and adatoms, rather than the misfit dislocation mechanism observed in Pd/Cu(100). The theoretical results for the average interlayer distance of the film and the in-plane strain for the top surface layers as a function of the film thickness are shown in figures 11 and 10, respectively. The theory again is in good agreement with the experimental data, indicating a stable highly strained epitaxial state below 9 ML.

The good agreement between the experimental data and the equilibrium simulation study leads us to conclude that the observed configurations of the film at different thicknesses correspond to equilibrium state with thermally generated misfit dislocations as the strain relief mechanism. The microscopic nature of the misfit dislocation observed here for the Pd/Cu(100) system is rather complicated and does not fit into the simple model postulated previously [28].

4. Strain relaxation through self-organized array of islands

In the previous sections we studied dislocations in the 'Frank-van der Merwe' (FM) morphology where the substrate is covered by a film of relatively uniform thickness. As an alternative way to release stress, the adsorbate sometimes splits into epitaxial nanoclusters, which are usually identified as adatom islands. Under the right circumstances these structures are known to self-assemble with a well-defined average spacing. The morphologies containing islands are classified in two categories, namely 'Volmer–Weber' (VW) and 'Stranski–Krastanov' (SK) modes. In the former category the substrate surface is uncovered except directly under the islands and in the latter the substrate is completely covered by a few complete layers, which coexist with islands. To include these strain relaxation mechanisms in our study, we take the 2D Lennard-Jones model as a starting point. Periodic boundary conditions are applied in the horizontal direction so that the simulation corresponds to a periodic arrangement of islands. The interactions are described by equation (1).

There are some essential methodological differences to the calculation involving the strain relaxation via the dislocation nucleation mechanism. The process that leads to island formation from an initial epitaxial state needs to overcome a much larger collection of energy barriers between metastable intermediate states in comparison to a typical dislocation nucleation. In principle a sequence of activation steps can be used to jump over any number of individual barriers. However, even in 2D the amount of possible sequences of activated transitions grows steeply with the sequence length and in the end the realistic atomistic evolution into islands becomes too difficult to handle by repeated activations. For this reason we do not simulate the island formation process. Instead, we start with a periodic array of possible island configurations and use molecular dynamics cooling to determine the minimum energy for a given island configuration. We then compare the ground state energies of all the configurations to determine the minimum energy configurations for a fixed coverage of the adsorbates. The physical restrictions we impose on the

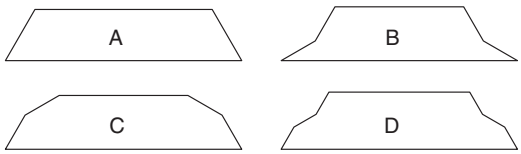

Figure 14. The minimum energy 2D island shapes among all of the concave, symmetrical configurations without overhangs or bulk vacancies are classified in four categories. Category A is a truncated pyramid shape. In other categories there is a short step located either to top (B), bottom (C) or middle (D) of the nonhorizontal island facets. The last category is seen only occasionally with large misfits. Reproduced from [29]. Copyright 2005 by the American Physical Society.

configurations are that the islands if they exist have to be coherent no dislocations or other imperfections, they must have a reflection symmetry about a line through the center and there are neither overhangs nor bulk vacancies. Each of these island configurations is described by a set of integer numbers, n_i specifying the number of atoms in successive island layers. For instance, the steep facets of an equilateral island would correspond to $n_i - n_{i+1} = 1$ in terms of these numbers. At this stage there are no restrictions on the facet orientations.

At low coverages, we find that practically all the lowest energy shapes are of truncated equilateral triangle type, such as the shape A in figure 14. All the actual facets are close-packed and the other, higher energy slopes are of shortest possible lengths, corresponding to $n_i - n_{i+1} = 3$. The locations of these slopes are most often at the corners such as the shapes B and C of figure 14, but sometimes they form additional terraces such as the shape D of figure 14. More limited tests with larger island sizes supported the same conclusion. In later studies we use only these shapes. It should be noted that since we are working in 2D, we do not see the distinctions between 1D grooves and nanoislands of higher-dimensional systems.

In the coverage range that we have studied ($\theta < 0.5$) we do not see dislocations within an individual island. Because we are using a local minimization technique, only those defects whose nucleation barrier is lower than what can be overcome by the numerical noise of the calculation can be present among the lowest energy states that we find. To study the dislocation nucleation in this context, we use the RBP approach as mentioned in the previous sections. In this case it is not necessary to speed up the activation by moving some conveniently preselected atoms to higher energies but the bias alone or in some cases a combination of the bias and a raise in the simulation temperature is enough to give the system a sufficient push. As has been reported in the literature, we see that the dislocations are nucleated at the corners where the island edges meet the substrate and that they glide along

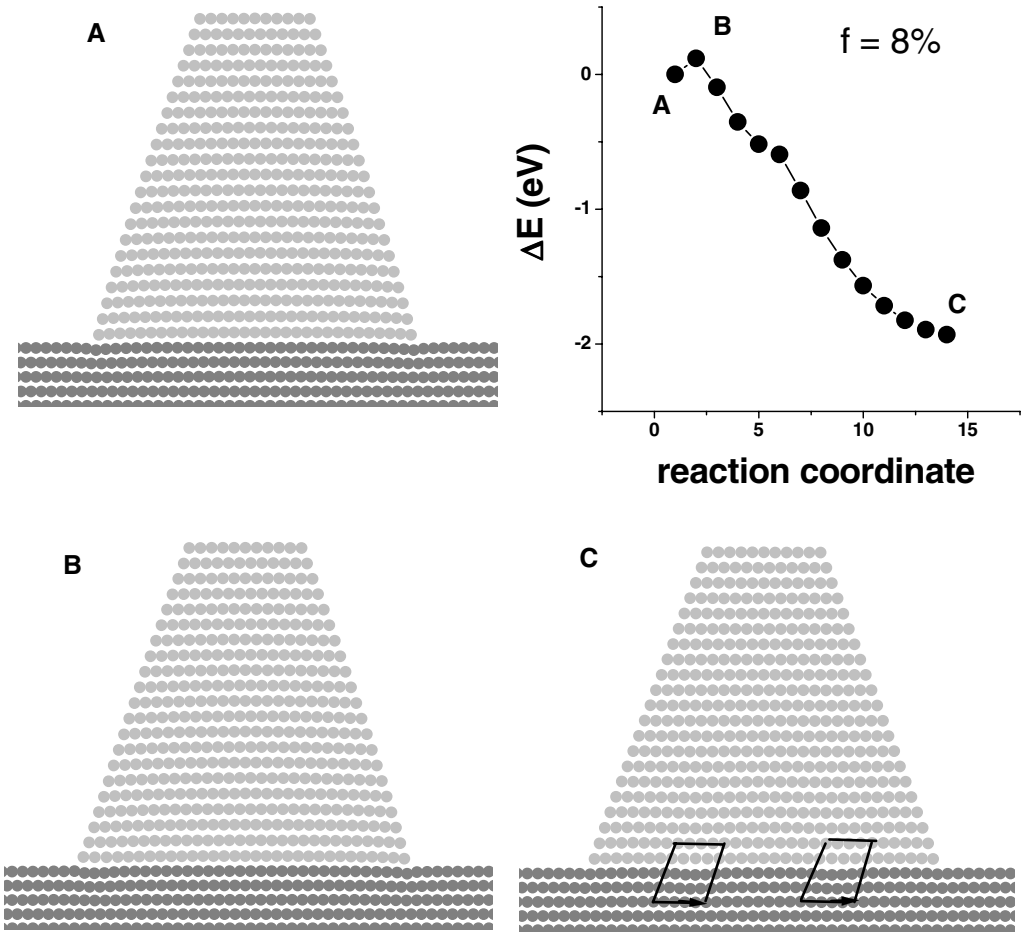

Figure 15. NEB minimum energy profile and particle configurations for a 411-atom strained island, where a pair of dislocations nucleate at the edges of the island. Closed paths in (c) are the Burgers circuits around the dislocation cores in the final state. Reproduced from [29]. Copyright 2005 by the American Physical Society.

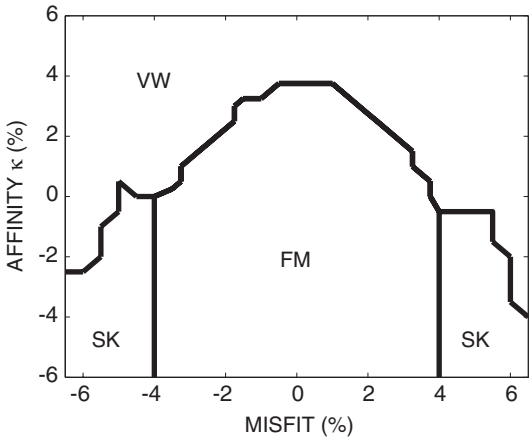

Figure 16. A diagram showing the dependence between the various growth modes on the substrate–adsorbate affinity κ and the lattice mismatch f. Negative affinity favors a large interfacial contact area. The coverage for this system is 4.1 full atomic layers. See the text for details. Reproduced from [29]. Copyright 2005 by the American Physical Society.

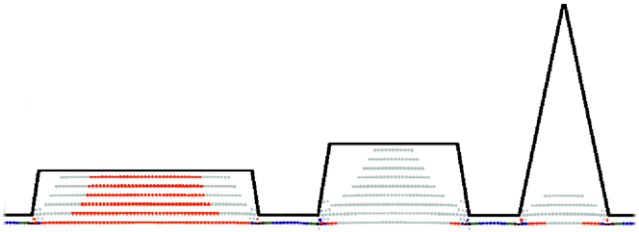

Figure 17. The relaxation pattern of small 'Stranski–Krastanov' islands for different aspect ratios. The contours of the islands are drawn with a black line. White corresponds to an unstrained state while the light gray and other colors of increasing contrast correspond to increasing levels of stress.

the island-substrate interface to the vicinity of the center. For details see in figure 15. The energy barrier of this process depends on the misfit and island size. For sufficiently large islands we do not need any activation procedure to get the defects, which hints that there is surface of critical island sizes and shapes such that outside the surface the defect nucleation barrier vanishes and the individual island is not a coherent structure.

In addition to misfit, the interaction potential allows the variation of the substrate–adsorbate affinity by tuning the relative strength of the interfacial bonds. This interfacial energy is the other key quantity which is thought to control the equilibrium morphology. In analogy with the misfit f, the potential depth ε in equation (1) for substrate–adsorbate interactions is set to $(1 - \kappa)$ times that of the adsorbate–adsorbate interactions. The negative values of the affinity κ put interfacial bonds in relative energetic advantage and the positive values do the converse. Our results show that the actual shapes of the islands are not affected, but the morphology of different island phases such as the SK or VW phases depend sensitively on the value of κ. With positive κ we get the flat configurations only when both coverage and misfit are small while with the negative κ we get islands only when both the coverage and misfit are large. We do not see SK configurations in the submonolayer coverages. To find these, we need to go to larger coverages where it is necessary to limit the number of possible facet orientations. For this purpose we fix the coverage and write down all configurations which satisfy the following assumptions. First, the adsorbate can have any number of complete atomic layers next to the substrate. Second, above the complete layers or directly on the substrate in case there are no complete layers, there can exist a single partial layer. Third, above the wetting films there can exist an island which has one of the shapes A, B or C. By sorting out the energy minimal configurations of this set for several combinations of misfit f and affinity κ; we can see how the preferential state of the adsorbate is influenced by these two properties. The resulting phase diagram in the κ and misfit f plane for a coverage of 4.1 monolayers is presented in figure 16. All three generic morphological categories are seen to be present in a parameter domain where both misfit and affinity magnitudes are $\leqslant 7\%$. The VW regime is seen both when affinity is positive and when misfit is large enough. The FM and SK modes, where adsorbate covers the whole substrate, are limited to a subdomain in the half-plane of negative affinity. The boundary of this domain is roughly a parabola, whose tip is close to $f = \kappa = 0$ and axis lies on the $f = 0$ line. This shows that the deformation energy grows proportional to the misfit squared, as the linear elasticity theory suggests. Roughly speaking, the VW mode begins when the stress energy of the substrate–adsorbate interface cancels the effect of negative affinity. Inside the parabola, the FM mode is limited to misfits less than $\approx 4\%$ and the rest of the domain belongs to the SK mode. Again, the sign of the misfit does not play a role. These borderlines between SK and FM are practically independent of the affinity. Intuitively the cross-over to the SK mode starts when the surface energy cost of an island is less than the stress energy of a planar film.

The island shape and size distribution in the SK mode is observed to be relatively narrow. In the literature this property is explained either by kinetic or equilibrium considerations. To address this question, we employ our methodology to scan the energy minimal island sizes and shapes for coverages up to ≈ 5 equivalent atomic layers.

To understand the strain relaxation in the SK phase, we show in figure 17 the strain relaxation patterns for a set of islands with different aspect ratios. The parameters correspond to a coverage of 2.5 complete layers and $\kappa = -4\%$. We note from these three geometries that the strain pattern are qualitative different for different aspect ratios. For the smallest aspect ratio, except for the surface and corner region, most of the atoms inside the island are strained. In the other limit of a large aspect ratio, except for the immediate adsorbate-substrate interface region, the bulk of the island is largely relaxed. Thus, the strain relaxation energy consideration favors sharp islands with large aspect ratio but the adsorbate-substrate interface bonding energy and the surface energy favor wide islands with small aspect ratios. The minimization of the total energy of the system leads to an optimal shape of the islands with an aspect ratio lying between 0.2 and 0.4 depending on the size of the

islands. When the coverage increases, the total strain energy can be lowered by allowing the size of the island to increase at the expense of reducing the thickness of the wetting film. The optimal size of the island results from the balance between the strain relaxation of larger island and the 'thinning' energies of the wetting film. Another factor that contribute to determining the optimal size of the island is the indirect interaction between the islands mediated by the substrate relaxation.

5. Conclusions

In this work, we have reviewed our recent atomistic studies of strain relaxation in heteroepitaxial systems.

First, we have developed a general scheme of identifying minimal energy paths for spontaneous generation of dislocations in heteroepitaxial systems. In contrast to finite-temperature MD techniques, with this scheme it is possible to systematically characterize the energetics and atomic mechanisms of strain relaxation in heteroepitaxial films. This approach requires no a priori assumptions about the nature of the transition path or the final states.

We find that the energy barrier for dislocation nucleation in strained epitaxial films decreases strongly with the misfit. The nucleation mechanism from a flat surface depends crucially on whether we start from a tensile or compressive initial state of the film. This asymmetry originates from the anharmonicity of the interaction potentials which leads to qualitatively different transition paths for the two types of strains. We have used model systems with a generalized Lennard-Jones interatomic potential to study strain relaxation in generic 2D systems as well as 3D systems with fcc(111) symmetry. For 3D systems, we have found that the lowest energy barriers correspond to two different cases: localized (stacking fault tetrahedra) and extended (ideal misfit dislocations) defects. An important result is that while the strain energy gain through the generation of a misfit dislocation is proportional to the length of the dislocation and hence the linear size of the system, the saddle point configuration is localized and hence the barrier for its generation is not an extensive quantity. Our results also further demonstrate a pronounced compressive-tensile asymmetry. All these results are in agreement with available experimental data. Furthermore, our study of the barriers for dislocation nucleation reveal nontrivial dependence on the range of the interatomic potential as a function of the misfit.

We have also done a more realistic study of strain relaxation in 3D Pd–Cu fcc(111) system using many-body EAM potential. The results confirmed qualitative features obtained for generic LJ system. In particular final states and saddle point configurations were similar to what we got for LJ system. However, certain quantitative details of the transitions differ considerably between the different types of interatomic potentials. In particular the actual value of the energy barrier for the transition is very different for different models.

Finally, we have also presented a combined experimental and theoretical study for the 3D heteroepitaxial Cu–Pd system on the fcc(100) surface [12], using realistic many-body EAM potentials and MD simulations. The theoretical results are in good agreement with the experimental observations, and explain correctly the observed tensile-compressive strain asymmetry.

In addition to dislocation generations, another channel for strain relaxation of the epitaxial films is through spontaneous generation of arrays of islands in the so-called 'Volmer–Weber' mode or the 'Stranski–Krastanov' mode. The theoretical understanding of this channel at present is not as advanced as the dislocation mechanisms. Even the question whether the island formation is dictated by equilibrium energy consideration or kinetic growth factors is not settled. In this work, we have presented a 2D study of this channel of strain relaxation through island formation based on equilibrium energy considerations. Our purpose is to gain an atomistic picture and obtain some qualitative understanding of this process. Indeed, we have been able to determine that the minimum energy configuration for a given coverage of the heteroepitaxial systems. The key factor leading to the minimum energy configuration is the competition of the strain relaxation energy in the island, the surface energies, the adsorbate-substrate interaction energy, the thinning energy of the wetting film beneath the island and the interaction energy between the islands. The minimization of the total energy including all these terms then leads to a periodic array of islands with an optimal size and shape. While the 2D study cannot be compare directly with the existing experimental data, the results are qualitatively similar to what has been observed in many heteroepitaxial systems. They demonstrate that equilibrium energy consideration is at least one viable driving mechanism for the formation of the island arrays.

Acknowledgments

This work has been supported by joint funding under EU STREP 016447 MagDot and NSF DMR Award No. 0502737. JJ and TA-N have also been supported in part by the Academy of Finland through its Center of Excellence COMP grant. EG was supported by Fundação de Amparo à Pesquisa do Estado de São Paulo-FAPESP (Grant no. 07/08492-9). We also acknowledge CSC-Center for Scientific Computing Ltd for allocation of computational resources.

References

[1] Campbell S A 2001 *The Science and Engineering of Microelctronic Fabrication* (New York: Oxford University Press)
[2] Luth H 1998 *Surfaces and Interfaces of Solid Materials* (Berlin: Springer)
[3] Bean J C 1985 *Science* **230** 127
[4] Matthews J W and Blakeslee A E 1974 *J. Cryst. Growth* **27** 118
[5] Ball C A B and van der Merwe J H 1983 *Dislocation in Solids* ed F R N Nabarro (Amsterdam: North-Holland)
[6] Trushin O, Granato E, Ying S-C, Salo P and Ala-Nissila T 2002 *Phys. Rev.* B **65** 241408
[7] Trushin O, Granato E, Ying S-C, Salo P and Ala-Nissila T 2002 *Phys. Status Solidi* b **232** 100
[8] Trushin O, Granato E, Ying S C, Salo P and Ala-Nissila T 2003 *Phys. Rev.* B **68** 155413
[9] Trushin O, Jalkanen J, Granato E, Ying S C and Ala-Nissila T 2008 unpublished

[10] Trushin O, Salo P, Ala-Nissila T and Ying S C 2004 *Phys. Rev.* B **69** 033405
[11] Jónsson H, Mills G and Jacobsen K W 1998 *Classical and Quantum Dynamics in Condensed Phase Simulations* ed B J Berne *et al* (Singapore: World Scientific)
[12] Yafeng Lu, Przybylski M, Trushin O, Wang W H, Barthel J, Granato E, Ying S C and Ala-Nissila T 2005 *Phys. Rev. Lett.* **94** 146105
[13] Rasmussen T 2000 *Phys. Rev.* B **62** 12664
[14] Voter A F, Montalenti F and Germann T C 2002 *Annu. Rev. Mater. Res.* **32** 321
[15] Dellago C, Bolhuis P G, Csajka F S and Chandler D 1998 *J. Chem. Phys.* **108** 1964
Dellago C, Bolhuis P G and Chandler D 1998 *J. Chem. Phys.* **108** 9236
[16] Berry J, Grant M and Elder K R 2006 *Phys. Rev.* E **73** 031609
[17] Chen L Y and Ying S C 1999 *Phys. Rev.* B **60** 16965
Chen L Y, Ying S C and Ala-Nissila T 2002 *Phys. Rev.* E **65** 042101
[18] Barkema G T and Mousseau N 1996 *Phys. Rev. Lett.* **77** 4358
[19] Henkelman G and Jónsson H 1999 *J. Chem. Phys.* **111** 7010
[20] Munro L J and Wales D J 1999 *Phys. Rev.* B **59** 3969
[21] Mousseau N and Barkema G T 2000 *Phys. Rev.* B **61** 1898
[22] Zhen S and Davies G J 1983 *Phys. Status Solidi* a **78** 595
[23] Dong L, Schnitker J, Smith R W and Srolovitz D J 1998 *J. Appl. Phys.* **83** 217
[24] Foiles S M, Baskes M I and Daw M S 1986 *Phys. Rev.* B **33** 7983
[25] Politi P, Grenet G, Marty A, Ponchet A and Villain J 2000 *Phys. Rep.* **324** 271
[26] Hirth J H and Lothe J 1968 *Theory of Dislocations* (New York: McGraw-Hill) p 780
[27] Howard D J, Bailey W E and Paine D C 1993 *Appl. Phys. Lett.* **63** 2893
[28] Müller B, Fischer B, Nedelmann L, Fricke A and Kern K 1996 *Phys. Rev. Lett.* **76** 2358
[29] Jalkanen J, Trushin O, Granato E, Ying S C and Ala-Nissila T 2005 *Phys. Rev.* B **72** 081403(R)